Floquet quantum many-body scars in the tilted Fermi-Hubbard chain

Jun-Yin Huang [1], Li-Li Ye [1], and Ying-Cheng Lai [1,2,*]
[1] School of Electrical, Computer and Energy Engineering, Arizona State University, Tempe, Arizona 85287, USA
[2] Department of Physics, Arizona State University, Tempe, Arizona 85287, USA

(Received 27 December 2024; revised 3 June 2025; accepted 23 June 2025; published 7 July 2025)

The one-dimensional tilted, periodically driven Fermi-Hubbard chain is a paradigm in the study of quantum many-body physics, particularly for solid-state systems. We uncover the emergence of Floquet scarring states, a class of quantum many-body scarring (QMBS) states that defy random thermalization. The underlying physical mechanism is identified to be the Floquet resonances between these degenerate Fock bases that can be connected by one hopping process. It is the first-order hopping perturbation effect. Utilizing the degenerate Floquet perturbation theory, we derive the exact conditions under which the exotic QMBS states emerge. Phenomena such as quantum revivals and subharmonic responses are also studied. Those results open the possibility of modulating and engineering solid-state quantum many-body systems to achieve nonergodicity.

DOI: 10.1103/4fpj-66gq

I. INTRODUCTION

Since the experimental observation of quantum revivals in Rydberg atom arrays [1], the phenomenon of quantum many-body scarring (QMBS) [2] has attracted a great deal of interest [3–22]. In general, QMBS states signify a weak breaking of ergodicity and thus a violation of the eigenstate thermalization hypothesis (ETH) [23,24] for quantum many-body interacting systems that are expected to thermalize and thus be ergodic [25]. A recent experimental work [26] showed that quantum revivals can be enhanced and stabilized via periodic driving, opening the possibility that QMBS can arise in quantum Floquet systems and raising the questions of whether QMBS states can arise in driven quantum systems in general. An affirmative answer would open the door to exploiting Floquet engineering for modulating and controlling the QMBS dynamics, and uncovering the underlying physical mechanism responsible for the emergence of Floquet scarring states then becomes an important issue. There were recent efforts in systems such as the driven PXP model [27–32], the Bose-Hubbard model [33–36], discrete-time crystals [37–39], and others [40–43]. For example, in the PXP model under some engineered driving protocols, a breakdown of the ETH was demonstrated and the Floquet scarring states were analyzed [27–29]. Most existing works on the Floquet scarring dynamics were based on the PXP model with engineered driving protocols.

The one-dimensional (1D) Fermi-Hubbard chain represents another paradigm for studying complex many-body physics, particularly in solid-state systems. Recently, experimental realization of the 1D titled Fermi-Hubbard chain was achieved by using cold atoms in a 3D optical lattice [44], providing a natural setting for investigating weak ergodicity breaking due to Hilbert space fragmentation [44–46]. It was also found that, beyond fragmentation, the 1D titled Fermi-Hubbard chain hosts QMBS states in some specific regime at half filling [17]. An outstanding question is whether Floquet scarring states can generally arise in the driven tilted Fermi-Hubbard systems. We note that, if the answer is affirmative, the cold-atom systems would provide a feasible experimental platform for verification, where the on-site Coulomb interaction strength can be readily controlled through a Feshbach resonance [33,47,48]. Another potential experimental system is the lattices of dopant-based quantum dots [49]. The Floquet tilted Fermi-Hubbard chain has thus become paradigmatic for studying quantum many-body phenomena. It is particularly appealing because of the potential feasibility of experimental implementation.

In this paper, we report Floquet scarring states in 1D tilted Fermi-Hubbard chains with periodically driven on-site Coulomb interaction, as illustrated by Fig. 1. First, we numerically identify the signatures of the possible Floquet scarring states according to the typical features of QMBS states in the static chain [17], which include persistent quantum revivals following quenches from some specific initial states, suppressed entanglement entropy, and the scarred tower structures in the overlaps of the Floquet eigenstates with some specific initial states. We find that the emergence of possible Floquet scarring dynamics are associated with robust synchrony of the quantum state with the driving frequency, regardless of its strength. In particular, the scarring dynamics periodically emerge as the static detuning term of the Coulomb interaction varies in integer multiples of the driving frequency. Then, exploiting the degenerate Floquet perturbation theory [27], we derive the analytic emergence conditions for the Floquet scarring states. It leads to the underlying mechanism: the Floquet scarring dynamics are the result of the resonances between these degenerate Fock bases that can be connected by one hopping process. That is, the resonances induced by first-order hopping perturbation lead to the Floquet scarring dynamics. We also find that, similar to the static chain, the equal quasienergy separation of the scarred towers is responsible for the observed quantum revivals [27,35]. The subharmonic and incommensurate responses of the revivals to driving are observed in distinct

*Contact author: Ying-Cheng.Lai@asu.edu

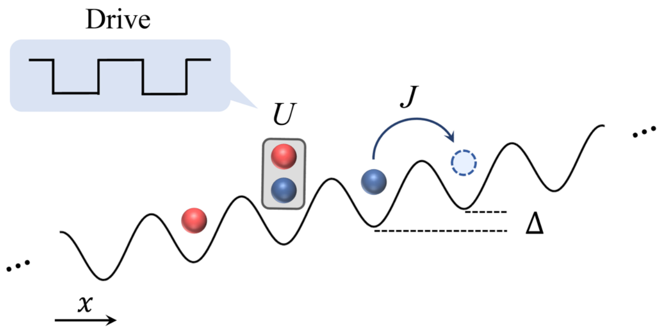

FIG. 1. A schematic illustration of the 1D tilted Fermi-Hubbard chain. The on-site Coulomb interaction is driven by a periodic signal: $U(t) = U_0 + U_m\,\mathrm{sgn}[\cos(\omega t)]$, where J is the nearest-neighbor hopping amplitude and Δ is a spin-independent tilted potential. The spin up (down) fermions are colored in red (blue).

frequency regimes. These responses and the synchronization effect open the door to modulating and engineering the Floquet scarring dynamics [31,32].

The resonance mechanism uncovered here is surprising, making it possible to heat up the system in a nonergodic manner. In general, Floquet resonances may lead to unbounded heating in many-body Floquet systems, thus a stable scarring state requires the absence of the resonances [41]. In Ising and Heisenberg interacting systems, it was found [41] that the resonances play a somewhat opposite role in the emergence of Floquet scarring states. In these systems, the emergence mechanism was found to be dynamical freezing under a strong driving. In particular, at so-called scar points, the longitudinal magnetization becomes an emerged conserved quantity, preventing the system from heating up ergodically. The resonances tend to destroy the inertness of the scar point, implying the emergence of stable Floquet scarring dynamics without such resonances. A similar role of resonances also was observed in the driven PXP model [27]. The reason for the seeming contradiction with our work lies in the nature of the unperturbed dynamics. In their system, the unperturbed systems can heat up ergodically, which is thermal. At scar points, the dynamics are severely constrained by the emergence of the local conserved quantity, while the resonances would significantly weaken the dynamical constraint. In our system, the unperturbed system does not thermalize because all the fermions are fully confined to their initial lattice sites. The resonances induced by the hopping perturbation then open the way to heat up. In addition, the resonances do not lead to unbounded heating, since the hopping amplitude is typically much smaller than on-site Coulomb interaction and tilted potential strength.

In Sec. II, we introduce the 1D driven tilted Fermi-Hubbard chain and describe the phenomenon of QMBS in the corresponding static chain. The Floquet scarring states are investigated in Sec. III, where the phenomenon of quantum revivals is studied in Sec. III A and the conditions dictating the emergence of the Floquet scarring states are obtained numerically in Sec. III B. An analytic derivation of the emergence conditions is presented in Sec. IV A based on the degenerate Floquet perturbation theory, and the connection between the undriven and Floquet QMBS dynamics is analyzed in Sec. IV B. The phenomena of subharmonic and incommensurate responses to driving are presented in Sec. V. A summary and discussion are given in Sec. VI. The methods for calculating the quantum evolution dynamics, bipartite von Neumann entanglement entropy, and an error analysis are provided in Appendix A. The transition from Wannier-Stark localization to Floquet scar phase is described in Appendix B. A detailed introduction to the Floquet perturbation theory is given in Appendix C and the robust period-doubling phenomenon is described in Appendix D.

II. 1D TILTED FERMI-HUBBARD CHAIN

The 1D tilted Fermi-Hubbard chain under periodic driving is given by the following Hamiltonian [17,44]:

$$H = \sum_{j,\sigma=\uparrow,\downarrow} (-J\hat{c}^{\dagger}_{j,\sigma}\hat{c}_{j+1,\sigma} + \mathrm{H.c.} + \Delta j \hat{n}_{j,\sigma}) + U(t)\sum_j \hat{n}_{j,\uparrow}\hat{n}_{j,\downarrow}, \tag{1}$$

where $\hat{c}^{\dagger}_{j,\sigma}$ ($\hat{c}_{j,\sigma}$) is the fermionic creation (annihilation) operator on site j with the spin index σ, $\hat{n}_{j,\sigma} = \hat{c}^{\dagger}_{j,\sigma}\hat{c}_{j,\sigma}$ is the density operator, J and Δ are the nearest-neighbor hopping amplitude and spin-independent tilted potential, respectively. For simplicity, the on-site Coulomb interaction is governed by a square-wave driving function: $U(t) = U_0 + U_m\,\mathrm{sgn}(\cos(\omega t))$, where U_0 is the static detuning, U_m is the modulation amplitude, and ω is the driving frequency. The linear static tilt Δ can be implemented using a magnetic field gradient and the time-periodic signal $U(t)$ can be modulated via a Feshbach resonance [33,47,48]. We assume that the the system has an even number L of sites, with the initial state containing equal numbers of spin-up and spin-down fermions [17]. Periodic boundary conditions are applied to eliminate the boundary effects.

To recognize Floquet scarring states, we describe QMBS states in the corresponding undriven system [17]. We use the following notations: $\uparrow$ for spin up, $\downarrow$ for spin down, 0 for an empty site, and $\updownarrow$ for a doublon. At the filling factor

$$\nu = (N_{\uparrow} + N_{\downarrow})/L = 1, \tag{2}$$

the undriven system hosts QMBS states in the regime $\Delta \approx U \gg J$, which can be conveniently probed using a quantum quench process from some special nonequilibrium initial states $|\psi_s\rangle$. Such initial states can be

$$|\downarrow\uparrow\uparrow\downarrow\cdots\rangle \quad \text{and} \quad |\downarrow\cdots\downarrow\updownarrow 0\uparrow\cdots\uparrow\rangle,$$

as well as their spin-reversed states:

$$|\uparrow\downarrow\downarrow\uparrow\cdots\rangle \quad \text{and} \quad |\uparrow\cdots\uparrow\updownarrow 0\downarrow\cdots\downarrow\rangle.$$

A salient feature of QMBS states is the fidelity revival observed during the time evolution that starts from the special initial states $|\psi_s\rangle$. The fidelity is characterized by the overlap between the time-evolved quantum state $|\psi(t)\rangle$ and its initial state $|\psi_0\rangle$, defined as

$$F(t) \equiv |\langle\psi(t)|\psi_0\rangle|^2. \tag{3}$$

Differing from previous work [17], we treat the full chain directly, following the numerical methods in Ref. [44]. The details are provided in Appendix A. For convenience, the hopping parameter and the Planck constant are normalized to $J \equiv 1$ and $\hbar \equiv 1$, respectively. We set the system size to $L = 8$. In an undriven chain, the revivals from the initial state

$$|\psi_s\rangle = |\downarrow\uparrow\uparrow\downarrow\downarrow\uparrow\uparrow\downarrow\rangle$$

are shown in blue in Fig. 2(a), where the revival period is $T_* \approx \sqrt{2}\pi$. The revivals are not perfect, where the height of the revival peak decreases with time. Another quantity characterizing the evolution of a quantum state is the bipartite von Neumann entanglement entropy $S_{N/2}$, which is suppressed in a quantum quench. Figure 2(b) plots $S_{L/2} = S_l = -\mathrm{tr}(\rho_l \log \rho_l)$ (blue), where the subscript l (r) denotes the left (right) half-chain, and $\rho_l(t) = \mathrm{tr}_r|\psi(t)\rangle\langle\psi(t)|$ is the reduced density matrix for the left subsystem by tracing out the right subsystem. The system eigenstates can be calculated by diagonalizing the Hamiltonian of the full chain in the standard Fock space. The overlap of eigenstates with the initial state $|\psi_s\rangle$ is shown in Fig. 2(c), demonstrating the scarred eigenstates [3] as marked by the scarred tower structures and the black dots at the top of the towers. These towers have a near-equal energy separation $\delta E \approx \sqrt{2}$, as the embedding construction in a thermal eigenstate. The scarred eigenstates have an abnormally high overlap with the initial state $|\psi_s\rangle$, resulting in the revivals in Fig. 2(a) with the revival period $T_* \approx 2\pi/\delta E$, i.e., $\omega_* \approx \delta E$.

Another type of nonequilibrium initial states at the filling factor $\nu = 1$ ($N_\uparrow = N_\downarrow = L/2$) is the so-called thermalized initial state, e.g.,

$$|\psi_{th}\rangle = |\uparrow\downarrow\uparrow\downarrow\uparrow\downarrow\uparrow\downarrow\rangle\,.$$

When quenched from $|\psi_{th}\rangle$, both the undriven and driven systems rapidly thermalize, as shown in Fig. 3. In particular, Fig. 3(a) shows that the fidelity quickly decreases to near zero values and remains at such values. Figure 3(b) shows that $S_{L/2}$ increases with time and rapidly becomes saturated.

III. EMERGENCE OF FLOQUET SCARRING STATES

A. Quantum revivals

Figure 2(a) presents an example of the phenomenon of quantum revivals, where the fidelity exhibits distinct peaks during the time evolution and the revival period is about twice of that for the undriven case: $T_r \approx 2T_*$. The results in Fig. 2(a) suggest that the periodic driving induces and enhances quantum revivals, as characterized by the higher revival amplitude in Fig. 2(a). Similarly, the entanglement entropy $S_{L/2}$ in the driven system is relatively lower, as shown in Fig. 2(b). It is worth noting that, for static detuning $U = U_0 = 4.4$, there is no revival of the initial state $|\psi_s\rangle$ due to the rapid thermalization, as exemplified in Fig. 4. Insights into the driven revival dynamics from $|\psi_s\rangle$ can be gained by studying the Floquet eigenstates. In particular, the periodically modulated Hamiltonian $H(t) = H(t + T)$ is determined by the time evolution of the Floquet operator over one period T [50]:

$$\mathcal{U}(t_0 + T, t_0) = \mathcal{T} \exp\left[-\mathrm{i}\int_{t_0}^{t_0+T} H(t)dt\right], \tag{4}$$

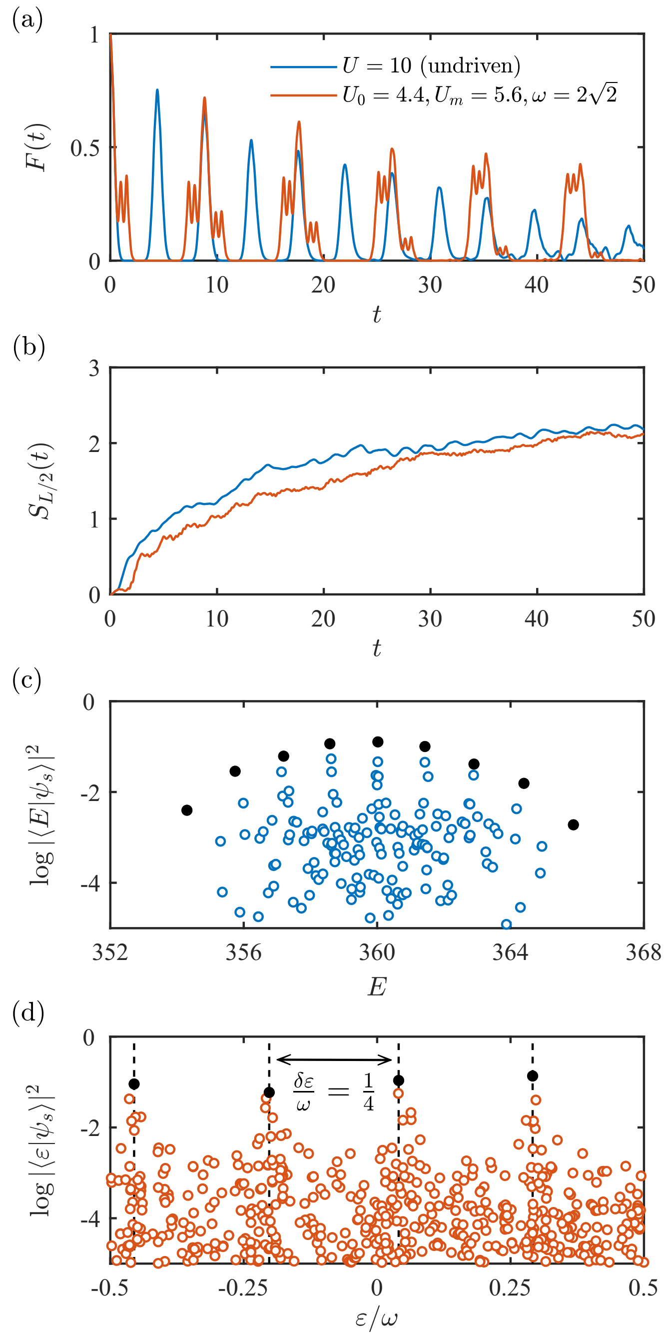

FIG. 2. Scarring dynamics in a quench process in the 1D tilted Fermi-Hubbard system. The initial state is $|\psi_s\rangle = |\downarrow\uparrow\uparrow\downarrow\downarrow\uparrow\uparrow\downarrow\rangle$. The system parameters are $L = 8$ and $\Delta = 10$. The undriven case for $U = 10$ is represented by the blue color, and the driven case by orange for $U_0 = 4.4$, $U_m = 5.6$, and $\omega = 2\sqrt{2}$. Time evolution of (a) wave function fidelity F and (b) bipartite entanglement entropy $S_{L/2}$. (c), (d) The overlap of the eigenstates and Floquet eigenstates with $|\psi_s\rangle$ for the undriven and driven cases, respectively, where the black dots indicate the top of every tower structures, corresponding to the scarring states in (c) and the Floquet scarring states in (d). These towers have an equal or approximately equal energy separation of about $\sqrt{2}$ in (c) and $\omega/4$ in (d).

where $\mathcal{T}$ denotes the time ordering and the initial time t_0 is set to 0. For square-wave driving, the Floquet operator

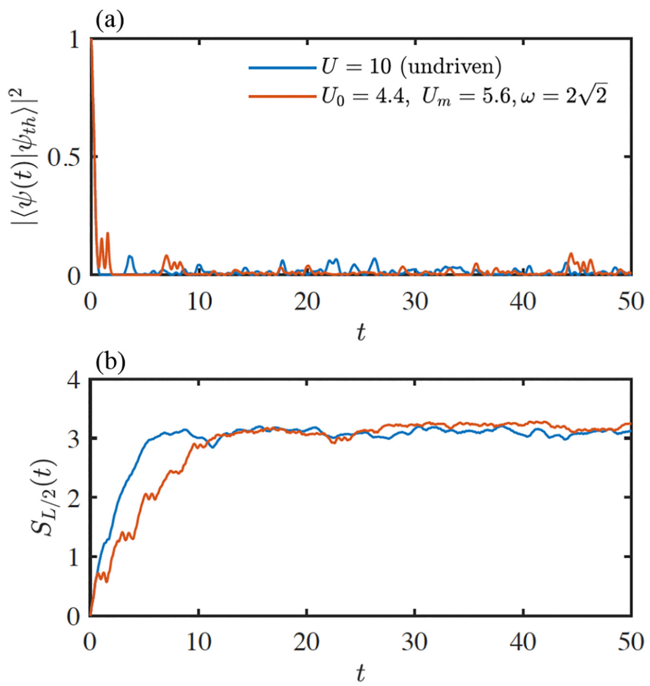

FIG. 3. Distinct dynamical behaviors following a quench from a thermalized initial state. The nonequilibrium initial state is given by $|\psi_{th}\rangle = |\uparrow\downarrow\uparrow\downarrow\uparrow\downarrow\uparrow\downarrow\rangle$. The undriven system has $U = 10$ and the Floquet has a square-wave driving $U(t) = U_0 + U_m \,\mathrm{sgn}[\cos(\omega t)] = 4.4 + 5.6 \,\mathrm{sgn}[\cos(2\sqrt{2}t)]$. (a) Time evolution of the wave function fidelity: Both the undriven and Floquet systems rapidly thermalize as the fidelity quickly decreases to zero without any revivals, and (b) $S_{L/2}$ increases and rapidly becomes saturated. Other system parameters are $L = 8$ and $\Delta = 10$.

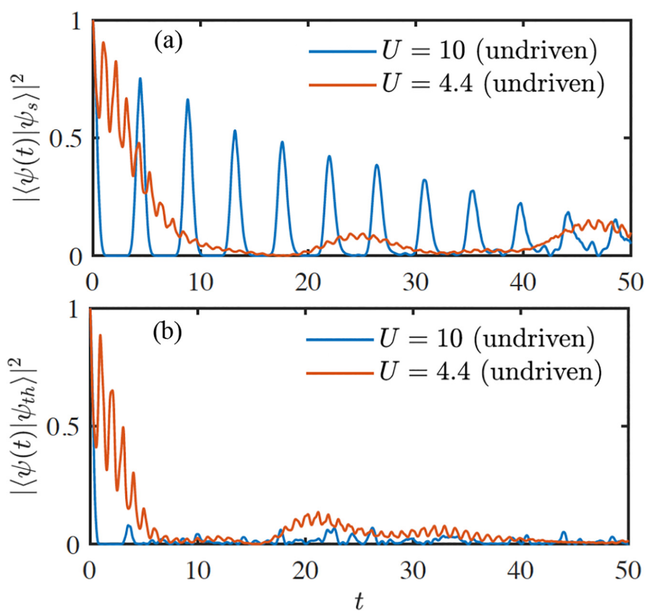

FIG. 4. Time evolution of the wave-function fidelity. The quantum state is quenched from (a) $|\psi_s\rangle$ and (b) $|\psi_{th}\rangle$ for two undriven cases with $U = 10$ (blue) and $U = 4.4$ (red). System parameter values are $L = 8$ and $\Delta = 10$.

becomes

$$\mathcal{U} = e^{-\mathrm{i}H_+T/4}e^{-\mathrm{i}H_-T/2}e^{-\mathrm{i}H_+T/4}, \tag{5}$$

where

$$H_\pm = H_s \pm U_m \sum_j \hat{n}_{j,\uparrow}\hat{n}_{j,\downarrow}, \tag{6}$$

with the static detuning Hamiltonian H_s. The Floquet operator is unitary with complex eigenvalues $\{e^{-\mathrm{i}\varepsilon_n T}\}$ and Floquet eigenstates $\{|n\rangle\}$. The quantities $\{\varepsilon_n\}$ are multivalued, whereas the quasienergies $\{\varepsilon_n \bmod \omega\}$ can be uniquely determined by a shift. Further, the time-independent stroboscopic Floquet Hamiltonian [50] H_F can be defined according to $\mathcal{U} = e^{-\mathrm{i}H_\mathrm{F}T}$, following $H_\mathrm{F}\,|n\rangle = \varepsilon_n\,|n\rangle$. The quasienergies and the Floquet eigenstates can be calculated through exact diagonalization of the Floquet operator $\mathcal{U}$ in the standard Fock space. For L sites and filling factor $\nu = 1$, the dimension of this space is

$$\binom{L}{L/2} \times \binom{L}{L/2}.$$

For $L = 8$, the dimension is 4900.

Figure 2(d) shows the overlap of the Floquet eigenstates with the initial state $|\psi_s\rangle$ for the same values of the driving parameters as in Fig. 2(a). The quasienergies fall within the interval $(-\omega/2, \omega/2)$ of the driving frequency, exhibiting four apparent tower structures with near-equal quasienergy separation $\delta\varepsilon \approx \omega/4 \approx \sqrt{2}/2$. The tops of these towers correspond to the Floquet scarring eigenstates, marked by the black dots. The strong overlaps are akin to the ones in Fig. 2(c). The equal quasienergy separation of the towers is responsible for quantum revivals: the quasienergy separation is equal to the revival frequency $\omega_r \approx \delta\varepsilon$ (a similar property was also noted previously [27,35]). Combining the relation $\delta E = 2\delta\varepsilon$, we obtain the doubling period $T_r \approx 2T_*$.

B. Emergence conditions of Floquet scarring states

To uncover the dependence of ω_r on the driving parameters, we search for potential Floquet scarring states. In particular, we fix $\Delta = 10$ and scan the parameter plane of U_0 and U_m to calculate the average fidelity for different driving frequencies:

$$\langle F\rangle_t = \frac{1}{\tau}\int_0^\tau F(t)dt, \tag{7}$$

where the upper integration bound τ is set as 50. In an approximate sense, the average fidelity characterizes the revivals. Note that a high value of the average fidelity is not necessarily indicative of revivals, as it may be the result of many-body localization or extremely slow thermalization. The following relative discrepancy of the average fidelity between different initial states provides a more appropriate way to characterize quantum revivals:

$$\varrho = \frac{\langle F_s\rangle_t - \langle F_{th}\rangle_t}{\langle F_{th}\rangle_t}, \tag{8}$$

where the subscripts s and th correspond to the initial state $|\psi_s\rangle$ and another one chosen as $|\psi_{th}\rangle = |\uparrow\downarrow\uparrow\downarrow\cdots\rangle$, respectively. The relative discrepancy ϱ in fact quantifies the degree

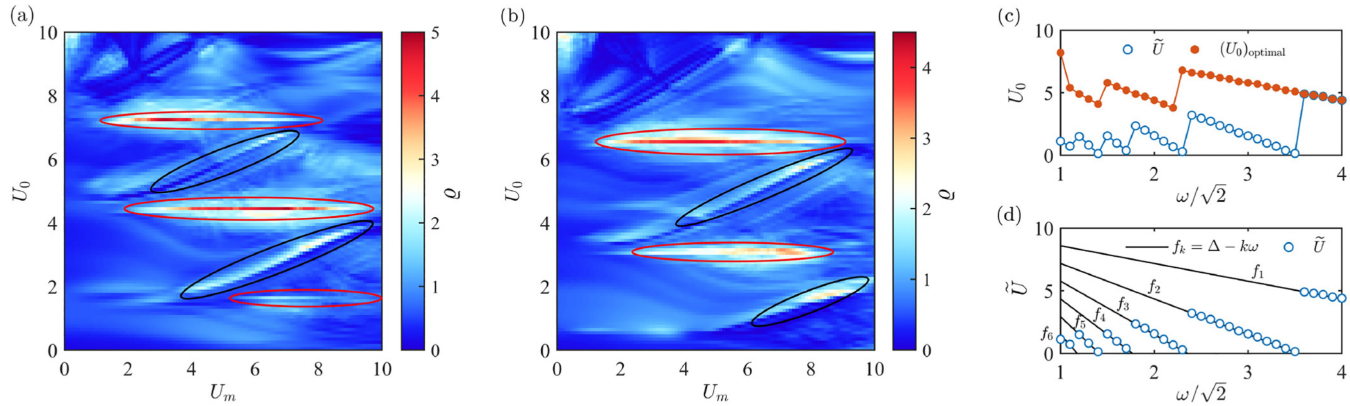

FIG. 5. Emergence of Floquet scarring in driven 1D tilted Fermi-Hubbard system. The system size is $L = 8$. (a), (b) Relative discrepancy ϱ of the average fidelity between two initial states $|\psi_s\rangle$ and $|\psi_{th}\rangle = |\uparrow\downarrow\uparrow\downarrow\uparrow\downarrow\uparrow\downarrow\rangle$ in the parameter plane (U_0, U_m). The average fidelity is calculated over the time interval [0,50]. The driving frequency is $\omega = 2\sqrt{2}$ for (a) and $\omega = 3.5$ for (b). The Floquet scarring states (encircled in red) appear at some specific values of U_0. The regions surrounded by the black curves correspond to the transition states. (c) The quantity $\widetilde{U}$ as the minimum threshold value for the emergence of the scarring dynamics (blue dots) and $(U_0)_{\mathrm{optimal}}$ corresponding to the maximal value of ϱ (red dots) for 31 discrete values of the driving frequency. (d) The quantity $\widetilde{U}$ characterized by a series of linear functions $f_k = \Delta - k\omega$, for $\Delta = 10$ and $k = 1, 2, \cdots, 6$.

of quantum revivals after removing the thermal decay behavior of quench from $|\psi_{th}\rangle$. Figures 5(a) and 5(b) show ϱ versus U_0 and U_m for two values of the driving frequency: $\omega = 2\sqrt{2}$ and $\omega = 3.5$, respectively, for $L = 8$. The regions with high ϱ values are encircled in red, in which Floquet scarring states arise. These states appear for some specific U_0 values (denoted as U_0^s) over a wide range of U_m, as indicated by the horizontal lines with bright red. The results suggest

$$U_0^s \approx \widetilde{U} + n\omega, \tag{9}$$

where $\widetilde{U}$ is the minimum threshold value for the emergence of the scarring dynamics for n being an integer and $\widetilde{U}$ depends only on the driving type and its frequency ω. The regions encircled by the black curves do not correspond to the Floquet scarring states, even though their ϱ values are not too small. In fact, in these regions, states are in a transition from Wannier-Stark localization to the Floquet scarring phase, where both the quantum fidelity quenching from $|\psi_s\rangle$ and $|\psi_{th}\rangle$ have large average values and oscillations, whereas the evolution of $|\psi_s\rangle$ revives without reaching zero. More details of the transition states are presented in Appendix B.

We further scan the independent parameter space of $U_0 \in [0, 10]$ and $U_m \in [0, 10]$ for 31 discrete driving frequencies $\omega = \sqrt{2}, 1.1\sqrt{2}, 1.2\sqrt{2}, \cdots, 4\sqrt{2}$. At each frequency, the optimal parameter is given by

$$(U_0)_{\mathrm{optimal}} = \arg\max_{U_0, U_m}\{\varrho(U_0, U_m)\}, \tag{10}$$

which corresponds to the most distinct scarring dynamics in the entire parameter plane (U_0, U_m), as shown in Fig. 5(c). The quantity ϱ is a function of parameters U_0 and U_m: $\varrho(U_0, U_m)$, where the argmax function in Eq. (10) optimizes over both U_0 and U_m. The threshold values of $\widetilde{U}$ can be obtained from Eq. (9), which decreases to zero linearly with increased ω and then attains a larger value. With respect to ϱ, the optimal parameter $(U_0)_{\mathrm{optimal}}$ has a similar behavior. The dependency of $\widetilde{U}$ on ω can be characterized by a series of linear functions:

$$\widetilde{U} = \Delta - k\omega, \tag{11}$$

for $k = 1, 2, 3, \cdots$, as shown in Fig. 5(d). Since $\widetilde{U}$ is the minimum U_0^s within the range $0 \leqslant U_0 \leqslant 10$, the integer k can be determined by $0 \leqslant \Delta - k\omega < \omega$ for specific driving frequency ω.

The relations (9) and (11) are the conditions under which the Floquet scarring states can emerge periodically over a wide range of the modulation amplitude U_m as the static detuning term U_0 varies. This signifies a resonance induced by the periodic driving, whose frequency is exactly the driving frequency. While the emergence of the Floquet scarring states has been illustrated using the analytically treatable case of discrete pulsed driving, the phenomenon occurs if the driving is sinusoidal, as shown in Figs. 6 and 7.

IV. ANALYTIC DERIVATION OF THE EMERGENCE CONDITIONS

A. Emergence conditions

The emergence of the Floquet scarring states, as stipulated by the conditions in Eqs. (9) and (11), are our main results. We now analytically derive these conditions from the degenerate Floquet perturbation theory [27,51]. To begin, we express the Hamiltonian (1) as $H(t) = H_0(t) + V$, where

$$H_0(t) = \Delta \sum_{j,\sigma=\uparrow,\downarrow} j\hat{n}_{j,\sigma} + U(t)\sum_j \hat{n}_{j,\uparrow}\hat{n}_{j,\downarrow},$$
$$V = -J\sum_{j,\sigma=\uparrow,\downarrow}(\hat{c}^\dagger_{j,\sigma}\hat{c}_{j+1,\sigma} + \mathrm{H.c.}). \tag{12}$$

In the standard Fock basis, $H_0(t)$ is a diagonal matrix and commutes with itself at different times, V is completely off-diagonal and can be regarded as a small time-independent perturbation due to the conditions $\Delta \gg J$ and $(U_0 + U_m) \gg J$.

In the unperturbed system $[H(t) = H_0(t)]$, the Floquet eigenstates are simply the Fock bases $|\mathrm{F}\rangle$, following $H(t)\,|\mathrm{F}_i\rangle = E_i(t)\,|\mathrm{F}_i\rangle$ with index i marking the ith Fock basis.

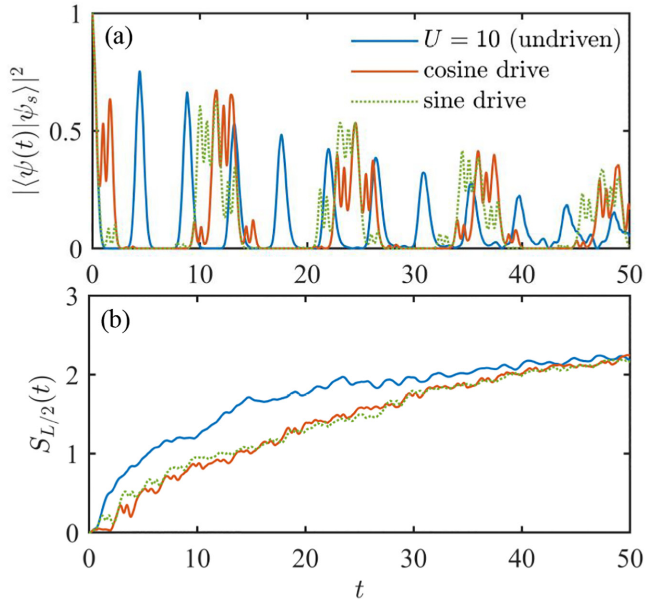

FIG. 6. Emergence of Floquet scarring states under sinusoidal driving. Shown is the time evolution of (a) wave-function fidelity and (b) entanglement entropy. The undriven, cosine drive, and sine drive cases are marked by blue, red, and green, respectively. System parameter values are $L = 8$ and $\Delta = 10$. On-site Coulomb interactions are $U = 0$ for undriven model, $U(t) = U_0 + U_m \cos(\omega t) = 4.4 + 5.6\cos(2\sqrt{2}t)$ for cosine drive, and $U(t) = 4.4 + 5.6\sin(2\sqrt{2}t)$ for sine drive.

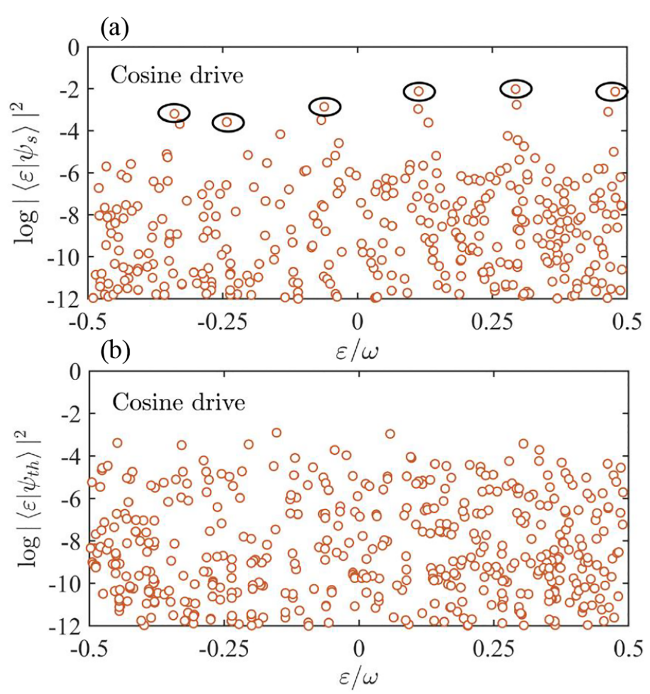

FIG. 7. Overlap of the Floquet eigenstates with the initial state under cosine driving. The initial state is (a) $|\psi_s\rangle$ and (b) $|\psi_{th}\rangle$. The driving parameter values are the same as those in Fig. 6. The system parameter values are $L = 8$ and $\Delta = 10$. The initial states are $|\psi_s\rangle = |\downarrow\uparrow\uparrow\downarrow\downarrow\uparrow\uparrow\downarrow\rangle$ and $|\psi_{th}\rangle = |\uparrow\downarrow\uparrow\downarrow\uparrow\downarrow\uparrow\downarrow\rangle$. The black dots indicate the top of each tower structure.

The Floquet modes are [50]

$$|\mathrm{F}_i(t)\rangle = e^{-\mathrm{i}\int_0^t dt' E_i(t')}\,|\mathrm{F}_i\rangle\,. \tag{13}$$

For $t = 0$, the Floquet modes are the Floquet eigenstates: $|\mathrm{F}_i(0)\rangle = |\mathrm{F}_i\rangle$. Intuitively, without the hopping perturbation V, the number of spin up (down) fermions at each site does not change with time and the energy varies in synchrony with the drive. In this case, the dynamics are fully constrained.

For small V, the Floquet modes start to hybridize and deviate from the unperturbed Floquet modes. Using Eq. (13), we expand the Floquet mode $|\mathrm{F}'_i(t)\rangle$ in the unperturbed eigenstates set [27] $\{|\mathrm{F}_i\rangle\}$:

$$|\mathrm{F}'_i(t)\rangle = e^{-\mathrm{i}\int_0^t dt' E_i(t')}\,|\mathrm{F}_i\rangle + \sum_{j\neq i} c_j(t) e^{-\mathrm{i}\int_0^t dt' E_j(t')}\,|\mathrm{F}_j\rangle\,, \tag{14}$$

where $c_j(t) \ll 1$ is of the order J/Δ for all $j \neq i$ and all t. The coefficients $c_j(t)$ characterize the small deviations from the unperturbed Floquet modes. For the perturbed eigenstate $|\mathrm{F}'_i\rangle$ at $t = 0$, we have [27]

$$c_j(0) = -\mathrm{i}\,\langle \mathrm{F}_j|V|\mathrm{F}_i\rangle\,\frac{\int_0^T dt\, e^{\mathrm{i}\int_0^t dt'[E_j(t')-E_i(t')]}}{e^{\mathrm{i}\int_0^T dt[E_j(t)-E_i(t)]}-1}. \tag{15}$$

More details about Eq. (15) can be found in Appendix C. The analysis so far holds for nondegenerate states. It breaks down when degeneracy occurs under the condition [52]

$$e^{\mathrm{i}\int_0^T dt[E_j(t)-E_i(t)]} = 1. \tag{16}$$

Suppose that there are p unperturbed eigenstates degenerate with a certain Fock basis $|\mathrm{F}_i\rangle$, satisfying the condition (16) for $|\mathrm{F}_i\rangle$. These p Fock bases can be denoted as $|\mathrm{F}_{ij}\rangle$ with $j = 1, 2, \cdots, p$, and $|\mathrm{F}_i\rangle \equiv |\mathrm{F}_{i0}\rangle$, following

$$H_0(t)\,|\mathrm{F}_{ij}\rangle = E_{ij}(t)\,|\mathrm{F}_{ij}\rangle$$

and $E_{i0}(t) = E_i(t)$, which form a degenerate set $\mathcal{D}_i = \{|\mathrm{F}_{ij}\rangle\,|\,j = 0, 1, \cdots, p\}$. From the degenerate perturbation theory [52], we disregard the expansion on the other unperturbed eigenstates. Any state in the perturbed degenerate set $\mathcal{D}'_i$ is then given by

$$|\mathrm{F}'_{ij}(t)\rangle = \sum_{j=0}^{p} c_j(t) e^{-\mathrm{i}\int_0^t dt' E_{ij}(t')}\,|\mathrm{F}_{ij}\rangle \tag{17}$$

at $t = 0$, where all $c_j(0)$ are of the order 1 (not the order J/Δ). As a result of first-order perturbation, the Floquet Hamiltonian H_F becomes [27]

$$(H_\mathrm{F})_{jj'} = \frac{\langle \mathrm{F}_{ij}|V|\mathrm{F}_{ij'}\rangle}{T}\int_0^T dt\, e^{\mathrm{i}\int_0^t dt'[E_{ij}(t')-E_{ij'}(t')]}, \tag{18}$$

where $j, j' = 0, 1, \cdots, p$, and details are in Appendix C.

In general, the scarring states, as some embedding constructions in the thermal eigenstates, are the result of an anomalously high overlap with the initial state, shown as the top of the tower structures in Figs. 2(c) and 2(d). For $L = 8$, the special initial state $|\psi_s\rangle = |\downarrow\uparrow\uparrow\downarrow\downarrow\uparrow\uparrow\downarrow\rangle$ is one of the Fock bases: $|\mathrm{F}_i\rangle = |\psi_s\rangle$. In the nondegenerate case, the overlap of the perturbed Floquet eigenstates with the initial state is

$$|\langle \mathrm{F}'_j|\mathrm{F}_i\rangle|^2 = \begin{cases} 1, & j = i \\ |c_i(0)|^2, & j \neq i. \end{cases}$$

According to Eq. (15), the overlap has an anomalously high value if and only if $j = i$, which does not allow the formation of scarred tower structures. Consequently, the Floquet scarring states can arise only in the degenerate case. Any state in $\mathcal{D}_i'$ may have an anomalously high overlap with $|\mathrm{F}_{i0}\rangle$, forming the scarred tower structure. It requires

$$\int_0^T dt[E_{ij}(t) - E_{ij'}(t)] = 2k\pi, \tag{19}$$

where k is an integer.

We next treat the degenerate set $\mathcal{D}_i$. Since $|\mathrm{F}_{i0}\rangle$ lacks doublon, its eigenenergy is $E_{i0} = \sum_{k=1}^{L} k\Delta$. Other Fock base states with the same eigenenergy (E_{i0}) must be degenerate with $|\mathrm{F}_{i0}\rangle$, whose number is

$$\binom{L}{L/2} - 1.$$

If $\mathcal{D}_i$ is entirely composed of the above $\binom{L}{L/2}$ Fock states, then H_F is just the zero matrix according to Eq. (18), since all the $\langle \mathrm{F}_{ij}|V|\mathrm{F}_{ij'}\rangle$ terms are zero. Then the eigenstates $|\mathrm{F}'_{ij}\rangle$ of H_F cannot have an anomalously high overlap with $|\mathrm{F}_{i0}\rangle$. To ensure that H_F has nonzero elements, $\mathcal{D}_i$ must be extended. In this regard, the Fock bases can be connected to $|\mathrm{F}_{i0}\rangle$ by one hopping process in $\mathcal{D}_i$. If the hopping

$$|\uparrow\downarrow\rangle \leftrightarrow |\updownarrow 0\rangle \leftrightarrow |\downarrow\uparrow\rangle$$

is allowed, the common eigenenergy of the Fock base states with one doublon is

$$E_{ij}(t) = U(t) - \Delta + \sum_{k=1}^{L} k\Delta.$$

The degenerate condition now is

$$\begin{aligned}\int_0^T dt[E_{i0}(t) - E_{ij}(t)] &= \int_0^T dt[\Delta - U(t)]\\ &= (\Delta - U_0)T\\ &= 2k\pi,\end{aligned} \tag{20}$$

i.e., $U_0 = \Delta - k\omega$, which is exactly the emergence conditions obtained from numerical calculations: Eqs. (9) and (11).

The above analysis provides some physical insights into the emergence of the Floquet scarring states. In the presence of a small hopping process, the Floquet eigenstates start to hybridize and deviate slightly from the Fock bases. The small deviations are characterized by $c_j(t)$ in Eq. (14), corresponding to the nondegenerate case. During the hybridization, the hopping between a series of degenerated unperturbed Floquet eigenstates can subject the system to heating up and exhibiting stable Floquet eigenstates with an anomalously high overlap with the initial state. The conclusion is that the Floquet scarring dynamics originate from the resonances between these degenerate Fock bases that can be connected by one hopping process.

B. From undriven to Floquet scarring states

To gain more insights into the emergence of Floquet scarring states, we explore the connection between undriven and Floquet scarring states. For the undriven system, scarring dynamics originate from a subgraph that is weakly connected to the rest of the Hamiltonian's adjacency graph [17]. The vertices of the adjacency graph consist of a series of Fock states that share the same energy as the initial state $|\psi_s\rangle$. When the system is quenched from $|\psi_s\rangle$, the wave function $|\psi(t)\rangle$ slowly leaks out of this subgraph over time. In the regime $\Delta \approx U \gg J$, the effective Hamiltonian [17] is

$$\begin{aligned}H_\mathrm{eff}^{+} = &-J \sum_{j,\sigma=\uparrow,\downarrow} \hat{c}_{j,\sigma}^{\dagger}\hat{c}_{j+1,\sigma}\hat{n}_{j,\bar{\sigma}}(1-\hat{n}_{j+1,\bar{\sigma}}) + \mathrm{H.c.}\\ &+ (U-\Delta)\sum_j \hat{n}_{j,\uparrow}\hat{n}_{j,\downarrow},\end{aligned} \tag{21}$$

where hopping to the left is allowed only if it increases the number of doublons. This dynamical confinement is the reason for the weakly connected subgraph. From the perturbation theory, we have that the degenerate set $\mathcal{D}_i$ of $|\psi_s\rangle$ constitutes the vertices in the adjacency graph and each edge connecting two vertices represents an allowed one hopping process.

In the corresponding Floquet system, similar processes occur. In particular, the adjacency graph now alternates over time due to the driving amplitude alternating between $U_0 + U_m$ and $U_0 - U_m$. Taking the driving protocol $U(t) = 4.4 + 5.6\,\mathrm{sgn}(\cos(2\sqrt{2}t))$ and $L = 6$ as an example, we find that the adjacency graph remains the same as that in the undriven case for $t < T/4$ or $t > 3T/4$. For $T/4 \leqslant t \leqslant 3T/4$, it is in the highly tilted regime $\Delta \gg |U_0 - U_m|, J$ with the effective Hamiltonian [44]

$$\begin{aligned}H_\mathrm{eff}^{-} = &J^{(3)}\hat{T}_3 + 2J^{(3)}\hat{T}_{XY} + 2J^{(3)}\sum_{j,\sigma}\hat{n}_{j,\sigma}\hat{n}_{j+1,\bar{\sigma}}\\ &+ (U_0 - U_m)\left(1 - \frac{4J^2}{\Delta^2}\right)\sum_j \hat{n}_{j,\uparrow}\hat{n}_{j,\downarrow},\end{aligned} \tag{22}$$

where $J^{(3)} = (U_0 - U_m)J^2/\Delta^2$ and

$$\hat{T}_3 = \sum_{j,\sigma} \hat{c}_{j,\sigma}\hat{c}_{j+1,\sigma}^{\dagger}\hat{c}_{j+1,\bar{\sigma}}^{\dagger}\hat{c}_{j+2,\bar{\sigma}} + \mathrm{H.c.},$$

$$\hat{T}_{XY} = \sum_{j,\sigma} \hat{c}_{j,\bar{\sigma}}^{\dagger}\hat{c}_{j+1,\bar{\sigma}}\hat{c}_{j+1,\sigma}^{\dagger}\hat{c}_{j,\sigma}.$$

In this case, all the Fock states without doublons constitute the vertices of the adjacency graph, as shown in Fig. 8. According to the Floquet theory, the effective adjacency graph is described by the Floquet Hamiltonian H_F, following

$$e^{-\mathrm{i}H_\mathrm{F}T} = e^{-\mathrm{i}H_\mathrm{eff}^{+}T/4}e^{-\mathrm{i}H_\mathrm{eff}^{-}T/2}e^{-\mathrm{i}H_\mathrm{eff}^{+}T/4},$$

which can be solved by Eq. (18) within the framework of degenerate Floquet perturbation theory, due to $[H_\mathrm{eff}^{+}, H_\mathrm{eff}^{-}] \neq 0$. The degenerate set $\mathcal{D}_i'$ consists of

$$\binom{L}{L/2} = 20.$$

Fock base states without doublons, 30 Fock states with one doublon $|\updownarrow 0\rangle$ segment, 12 Fock states with two doublon $|\updownarrow 0\rangle$ segments, and $|\updownarrow 0 \updownarrow 0 \updownarrow 0\rangle$. The effective adjacency graph is similar to the one for the undriven system and the driving parameters (U_0, U_m, ω) determine the weights of the edges according to Eq. (18).

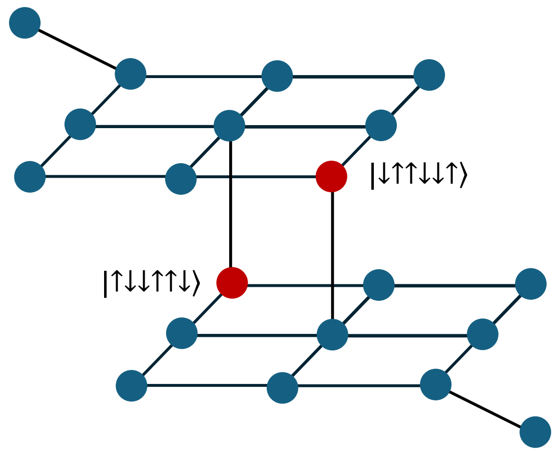

FIG. 8. Adjacency graph of the effective Hamiltonian for the undriven system with $L = 6$ in the highly tilted regime $\Delta \gg |U|, J$. The red vertices are $|\psi_s\rangle$: $|\downarrow\uparrow\uparrow\downarrow\downarrow\uparrow\rangle$ and $|\uparrow\downarrow\downarrow\uparrow\uparrow\downarrow\rangle$. The blue vertices are the other Fock states without doublon.

For the Floquet QMBS states, the emergence conditions are given by $U_0 = \Delta - k\omega$, where k is an integer. In the limit of $U_m \to 0$, the Floquet dynamics converge to the undriven dynamics with $U = U_0$, regardless of the value of ω, as illustrated by the blue and red curves in Fig. 9(a). The undriven QMBS states can be viewed as an emergence at $U_0 = \Delta = 10$ and $k = 0$. The emergence condition induces the resonances between vertices in the adjacency graph, facilitating weak ergodicity breaking. The parameters $(J, \Delta, \nu, U_m, \omega)$ determine the edges and weights among different vertices, thereby influencing the Floquet QMBS dynamics. The Floquet QMBS states include but extend far beyond the undriven one, and our emergence conditions offer a perspective on both Floquet and undriven QMBS dynamics.

We have obtained numerical results of the scarring states in both undriven and driven systems. For $U_0 = 10$ and U_m near zero, the Floquet scarring states persist, in agreement with our emergence condition. The variation of ϱ as a function of U_m is presented in Fig. 9(b), where a relatively high value of ϱ (e.g., $\varrho > 2$) signifies a pronounced revival. Approximately, the Floquet scarring states arise for $U_m \in [0, 1.3]$. For $U_0 = 10$ and $\omega = 4$, Figs. 9(c) and 9(d) present the deformation of the overlapping quantities $|\langle\varepsilon|\psi_s\rangle|^2$ and $|\langle\varepsilon|\psi_{th}\rangle|^2$, respectively, as U_m increases from 0.01 (undriven) to 10. The heights of the three most pronounced overlaps $|\langle\varepsilon|\psi_s\rangle|^2$ for $U_m = 0.01$ continuously decrease as U_m increases but they are still at a relatively high level for $U_m \in [0, 1.3]$, suggesting the robustness of the corresponding Floquet scarring states.

A remark is in order. The degeneracy condition Eq. (16) originates from the degenerate Floquet perturbation theory [34] for the driven PXP model. In this system, the driving protocol in one period $T = 2\pi/\omega$ is

$$H(t) = \begin{cases} H_{\rm PXP} + \lambda \sum_i n_i, & t \leqslant T/2 \\ H_{\rm PXP} - \lambda \sum_i n_i, & t > T/2, \end{cases}$$

where λ is the driving amplitude and n_i is the density of excitations on site i. It was found [34] that, in the vicinity of the degenerate condition ($\lambda/\hbar\omega = 2k$ with nonzero integers k), the dynamics are controlled by the non-PXP terms in

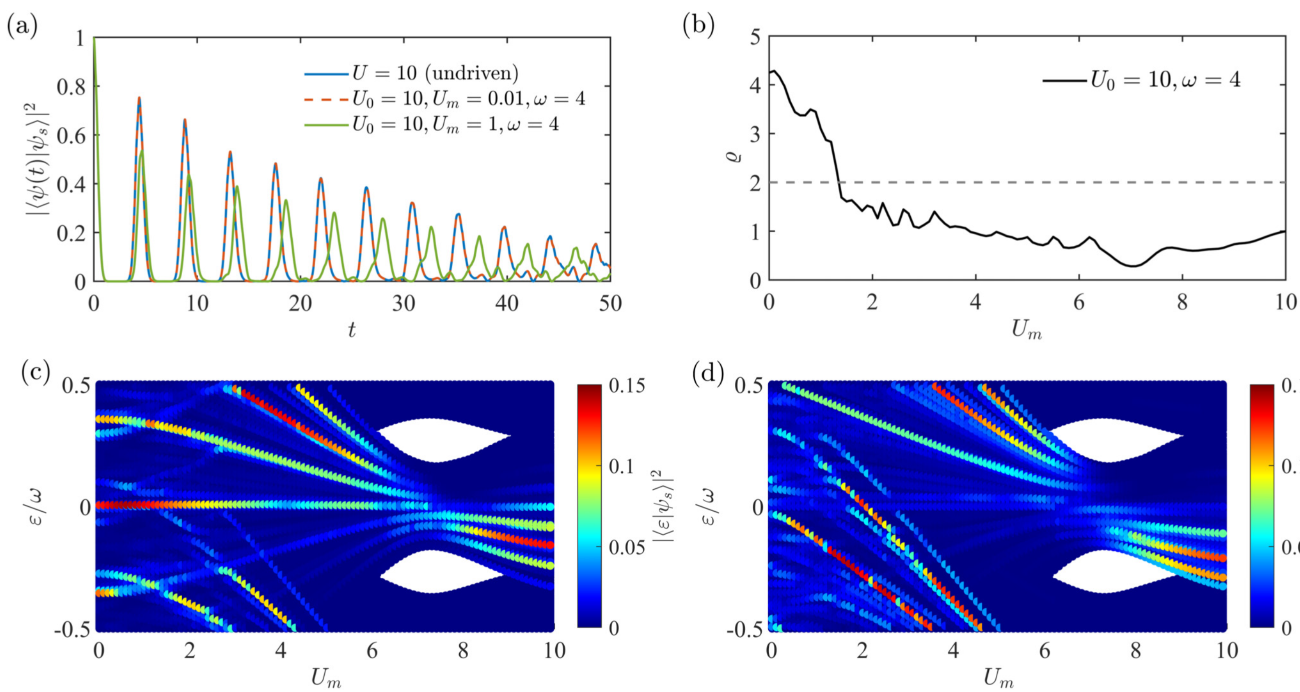

FIG. 9. From undriven scarring states to Floquet scarring states with driving parameters $U_0 = 10$ and $\omega = 4$. (a) Time evolution of the wave-function fidelity quenched from $|\psi_s\rangle = |\downarrow\uparrow\uparrow\downarrow\downarrow\uparrow\uparrow\downarrow\rangle$ for $U = 10$ (blue), $U(t) = 10 + 0.01\ \mathrm{sgn}(\cos(4t))$ (red), and $U(t) = 10 + 1\ \mathrm{sgn}(\cos(4t))$ (green). (b) Relative discrepancy ϱ of the average fidelity between $|\psi_s\rangle$ and $|\psi_{th}\rangle$ as a function of U_m. (c), (d) Overlaps of the Floquet eigenstates with the initial state as U_m varies from 0.01 to 10.

the Floquet Hamiltonian, which do not support scars. That is, the degenerate condition (or the resonances between the unperturbed degenerated bases) leads to a reentrant transition from weak ergodicity breaking to the ergodic regimes. It was found subsequently [41] that the degenerate condition plays a similar role in a periodically driven, interacting, nonintegrable Ising chain: the degenerate condition (or resonance) tends to destroy the scars, suggesting the possible emergence of stable Floquet scarring dynamics in the absence of resonances. However, in our driven tilted Fermi-Hubbard chain, the resonances play a somewhat opposite role in the emergence of Floquet scarring states. The contradiction can be attributed to the nature of the unperturbed dynamics. In particular, in the PXP model, ergodic heating occurs in the unperturbed system. The Floquet QMBS dynamics are constrained by the emergence of the local conserved quantity, while the resonances would significantly weaken such dynamical constraint. In the tilted Fermi-Hubbard chain, the fermions are fully confined to their initial lattice sites, so the unperturbed system does not thermalize. In this case, the resonances induced by the hopping perturbation make the system susceptible to weak ergodicity breaking.

V. SUBHARMONIC AND INCOMMENSURATE RESPONSES

Figures 2(a) and 2(d) show a fourth subharmonic response, a phenomenon reported in the discrete time crystal [37], where the driven revival frequency is a quarter of the driving frequency: $\omega_r \approx \omega/4$. In the 1D PXP model [26,31], under a driven chemical potential, when the initial state is the Néel state, a robust (second) subharmonic locking of the scarring frequency $\omega_r \approx \omega/2$ arises over a wide range of the driving frequency [26]. In fact, the driven revival frequency is a function of ω, U_0, and U_m, including harmonic, subharmonic, the forth subharmonic, etc., and even incommensurate responses. From the point of view of control and modulation, this implies a high degree of tunability.

We examine the parameter plane (ω, U_m) for the driven revival frequency at $U_0 = (U_0)_{\text{optimal}}$, which can be obtained as $\omega_r = \arg\max_\omega [f(\omega)]$, where

$$f(\omega) = \int_0^\tau F(t)e^{-i\omega t}dt \tag{23}$$

is the Fourier transform of $F(t)$ (we set $\tau = 100$ in numerical calculation). Figure 10(a) shows the relative discrepancy ϱ as a function of ω and U_m for $U_0 = (U_0)_{\text{optimal}}$. In the frequency domain, a higher amplitude $f(\omega_r)$ always corresponds to narrower broadening at ω_r, indicating higher revival peaks and more stable revival frequency, suggesting that the value of $f(\omega_r)$ can be used to characterize the strength of the quantum revivals. The contour line of $f(\omega_r) = 1$ is plotted in black chain curve. The frequency of the undriven revivals, $f(w_*) = 16.12$, serves as a reference point.

Figure 10(b) shows the actual dependence of the revival frequency ω_r on ω and U_m for $U_0 = (U_0)_{\text{optimal}}$, where the regions with high ϱ correspond to the typical scarring dynamics. The regions with low ϱ values ($\varrho < 1$) can then be disregarded, shown as the blank area with boundaries marked by the black chain curves. As $(U_0)_{\text{optimal}}$ abruptly changes its

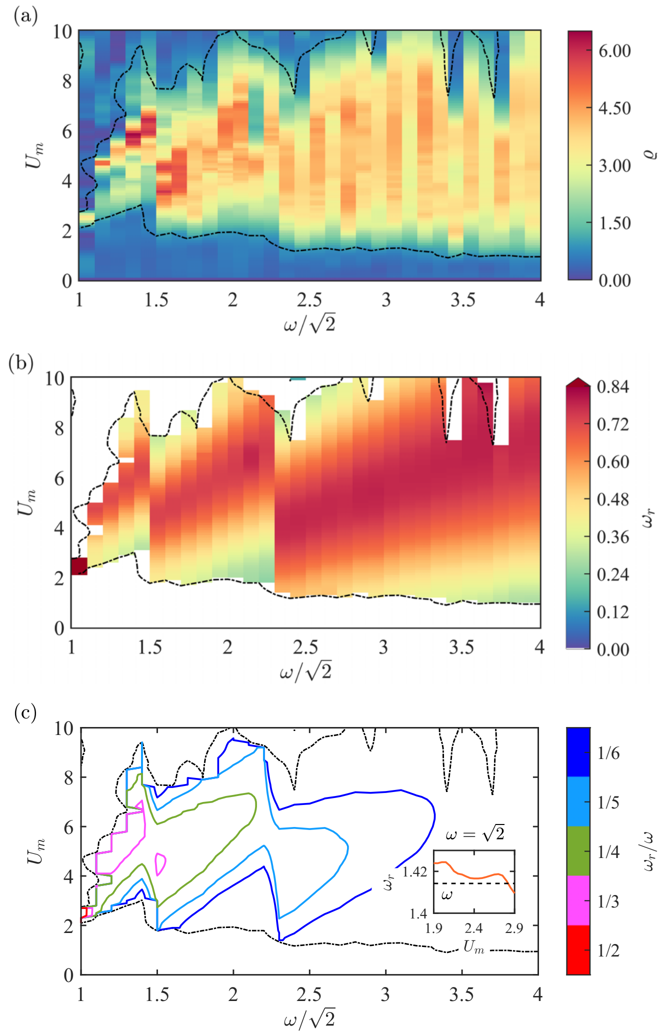

FIG. 10. Quantum revival properties of scarring dynamics in the driven 1D tilted Fermi-Hubbard systems. The emergence of the scarring states depends on the modulation amplitude U_m and the driving frequency ω. The system parameters are $L = 8$ and $U_0 = (U_0)_{\text{optimal}}$. The color scales indicate (a) the relative discrepancy ϱ, (b) the revival frequency ω_r, and (c) the orders of subharmonic response.

value at $\omega/\sqrt{2} = 1.1$, 1.5, and 2.3 [Fig. 5(c)], the changes in ω_r are discontinuous at these driving frequencies. The modulation amplitude U_m tends to shift toward a larger value when $(U_0)_{\text{optimal}}$ switches to a larger value. For $\omega = \sqrt{2}$, the scarring region follows $\omega_r \geqslant 0.84$ as marked by the same color (deep red). Figure 10(c) shows the contour lines representing a commensurate relation between ω_r and ω, including the second, third, …, and sixth subharmonic responses, i.e., $\omega_r = \omega/k$ with $k = 2, 3, \cdots, 6$, marked in different colors with the harmonic response ($\omega_r = \omega$) at $\omega = \sqrt{2}$ shown in the subgraph. An incommensurate relation can be realized in the regions between the adjacent contour lines. A convenient method to regulate these responses is fixing the driving frequency ω (with the corresponding U_0) and then tuning U_m, the so-called engineering subharmonic response via Floquet scarring states [32].

VI. DISCUSSION

In complex quantum systems, many-body interactions naturally lead to thermalization that destroys the coherence of the quantum states. However, QMBS states represent an exception with significant potential applications, e.g., in quantum information science and technology. The phenomenon of QMBS has attracted a great deal of recent attention. From an application perspective, driven systems are of particular interest because of the possibility of realizing quantum control and engineering through some external driving input. In a periodically driven system, the QMBS states become the Floquet scarring states that have mostly been investigated using the PXP model that is specific to the Rydberg atomic systems. A field in which many-body interactions are fundamental is solid-state systems that are often more accessible to control and device engineering, rendering useful and important studying the phenomenon of Floquet scarring in these systems. A paradigm for probing into Fermionic many-body physics in these systems is the 1D Fermi-Hubbard chain.

Here, we studied the 1D tilted Fermi-Hubbard system under periodic driving, motivated by the following considerations. Most existing studies on Floquet scarring focused on the PXP model under various engineered driving protocols. Whether QMBS states can emerge in general driven quantum systems and the underlying mechanisms remain open issues. For example, beyond known QMBS models such as the PXP model and the spin-1 XY model, distinct types of Floquet QMBS states may arise in other driven many-body systems and uncovering the emergence mechanisms could provide deeper insights into Floquet QMBS and broaden the applications of Floquet engineering in controlling quantum many-body dynamics. As a paradigmatic quantum many-body model, the 1D tilted Fermi-Hubbard chains was argued to host QMBS states [17], providing an ideal experimental platform for studying weak ergodicity breaking [44]. We asked the question of whether Floquet QMBS states can emerge in this system. Given its rich many-body physics and the recent experimental realization in cold-atom systems, this model provides an excellent platform for studying the interplay between periodic driving and weak ergodicity breaking. Investigating Floquet QMBS in this system would not only extend our understanding of nonequilibrium many-body dynamics beyond the PXP model but also offer insights into how periodic driving can stabilize or enhance quantum coherence in interacting systems. Furthermore, the tunability of interactions in cold-atom experiments via Feshbach resonances makes this system particularly suitable for experimental verification, offering a promising direction for Floquet engineering of quantum many-body states.

The 1D tilted static Fermi-Hubbard chain hosts QMBS states in a typical parameter regime [17]. The scarring dynamics follow a quench from some special initial states and their spin-reversed states. Our computations and analysis provide unequivocal evidence for the emergence of the Floquet scarring states in the systems with physical manifestations including persistent quantum revivals, suppressed entanglement entropy, and the scarred tower structures in the overlaps of Floquet eigenstates with the initial state. A unique feature of the towers is that they have an equal quasienergy separation that is approximately the revival frequency. This feature is associated with the wave function fidelity undergoing a constructive (or destructive) process to reach the local maximum (or minimum), similar to the previous explanation (Supplemental Material IV in Ref. [35]). Further, there are subharmonic and incommensurate responses of the revivals to driving.

The main contribution of our work is the discovery of the conditions under which the Floquet scarring states emerge. The general conditions were obtained through a systematic probe of the parameter space defining the driving signal, revealing that these states are the result of a synchrony between the static detuning and the driving frequency. An application of the degenerate Floquet perturbation theory allowed us to analytically derive the emergence conditions. Theoretical analysis revealed that the Floquet scarring states originate from the resonances between these degenerate Fock base states that can be connected through a one hopping process. The resonances are induced by the first-order perturbation effect, weakening the constraint in the unperturbed dynamics. Floquet scarring states are of fundamental importance to many-body physics with significant applications in quantum control and engineering. Our work provides a stepping stone for further analyzing the breakdown of the ETH in solid-state systems and a more rigorous understanding of the Floquet scarring states.

ACKNOWLEDGMENTS

We thank Prof. L. Ying for discussions. This work was supported by the Air Force Office of Scientific Research under Grant No. FA9550-21-1-0186 and by the Office of Naval Research under Grant No. N00014-24-1-2548.

DATA AVAILABILITY

The data that support the findings of this article are openly available [53].

APPENDIX A: QUANTUM DYNAMICAL EVOLUTION AND RELATED PHYSICAL QUANTITIES

1. Quantum evolution dynamics

We reduce the dimension of the Hamiltonian Hilbert space following the method in Ref. [44]. For fixed numbers of spin-up ($N_\uparrow$) and spin-down ($N_\downarrow$) fermions in a lattice of L sites, the number of spin σ bases is

$$d_\sigma = \binom{L}{N_\sigma}. \tag{A1}$$

Denoting the occupation sites of the spin-up and spin-down fermions as $\{i_1, i_2, \cdots i_{N_\uparrow},\}$ and $\{j_1, j_2, \cdots, j_{N_\downarrow}\}$, respectively, we obtain the typical number state as

$$|\psi\rangle = \hat{c}_{i_1,\uparrow}\hat{c}_{i_2,\uparrow}\cdots\hat{c}_{i_{N_\uparrow},\uparrow}\hat{c}_{j_1,\downarrow}\hat{c}_{j_2,\downarrow}\cdots\hat{c}_{j_{N_\downarrow},\downarrow}|0\rangle. \tag{A2}$$

The state can be represented by a pair of tuples $(\alpha, \beta) \equiv ((i_1, i_2, \cdots i_{N_\uparrow}), (j_1, j_2, \cdots, j_{N_\downarrow}))$ with the ordering $1 \leqslant i_1 < i_2 < \cdots < i_{N_\uparrow} \leqslant L$ and $1 \leqslant j_1 < j_2 < \cdots < j_{N_\downarrow} \leqslant L$. The number of full basis is thus $d_\uparrow \times d_\downarrow$ and a state is given by

$$|\psi\rangle = \sum_{\alpha,\beta} |\alpha,\beta\rangle\langle\alpha,\beta|\psi\rangle \equiv \sum_{\alpha,\beta} M^{(\psi)}_{\alpha\beta}|\alpha,\beta\rangle, \tag{A3}$$

where $M^{(\psi)}$ is a $d_\uparrow \times d_\downarrow$ matrix, and $|\alpha,\beta\rangle$ is the full basis corresponding to the tuple pair (α,β). The Hamiltonian becomes

$$H = H^{\text{hop}}_\uparrow \otimes \mathbb{1}_\downarrow + \mathbb{1}_\uparrow \otimes H^{\text{hop}}_\downarrow + H^{\text{diag}}, \tag{A4}$$

where $\mathbb{1}_\sigma$ is the $d_\sigma \times d_\sigma$ unit matrix,

$$H^{\text{hop}}_\sigma = \sum_i \hat{c}^\dagger_{i,\sigma}\hat{c}_{i+1,\sigma} + \text{H.c.}$$

is the $d_\sigma \times d_\sigma$ matrix, and H^{diag} is a $d_\uparrow d_\downarrow \times d_\uparrow d_\downarrow$ diagonal matrix. Defining the $d_\uparrow \times d_\downarrow$ matrix $F \equiv \text{diag}(H^{\text{diag}})$ with the elements

$$F_{\alpha\beta} = \left(\sum_{k=1}^{N_\uparrow} i_k + \sum_{k=1}^{N_\downarrow} j_k\right)\Delta + UN_d, \tag{A5}$$

where

$$N_d = |(i_1, i_2, \cdots i_{N_\uparrow}) \cap (j_1, j_2, \cdots, j_{N_\downarrow})|$$

is the number of the doublons, we obtain the Schrödinger equation as

$$\mathrm{i}\sum_{\alpha,\beta}\frac{\partial M^{(\psi)}_{\alpha\beta}}{\partial t}|\alpha,\beta\rangle = (H^{\text{hop}}_\uparrow \otimes \mathbb{1}_\downarrow + \mathbb{1}_\uparrow \otimes H^{\text{hop}}_\downarrow + F) \cdot \sum_{\alpha,\beta} M^{(\psi)}_{\alpha\beta}|\alpha,\beta\rangle, \tag{A6}$$

i.e.,

$$\mathrm{i}\partial M^{(\psi)}/\partial t = H^{\text{hop}}_\uparrow M^{(\psi)} + M^{(\psi)} H^{\text{hop}}_\downarrow + F \circ M^{(\psi)}, \tag{A7}$$

where $\circ$ represents the element-by-element multiplication (Hadamard product). An application of the Trotter-Suzuki decomposition stipulates that the dynamical evolution of the initial state is described by

$$M^{(\psi)}(t+\delta t) \approx e^{-\mathrm{i}\delta t\circ F} \circ e^{-\mathrm{i}\delta t H^{\text{hop}}_\uparrow} M^{(\psi)}(t) e^{-\mathrm{i}\delta t H^{\text{hop}}_\downarrow}, \tag{A8}$$

where the matrices F, $H^{\text{hop}}_\uparrow$, and $H^{\text{hop}}_\downarrow$ are all time dependent and $e^{-\mathrm{i}\delta t\circ F}$ is the element-wise exponentiation. As a result, the matrix computation has been reduced from the $d_\uparrow d_\downarrow \times d_\uparrow d_\downarrow$ dimension to the $d_\uparrow \times d_\downarrow$ dimension.

2. Bipartite von Neumann entanglement entropy and error analysis

The basis numbers for the left and right half-chains are d_l and d_r, respectively. A typical quantum state is

$$|\psi\rangle = \sum_{l,r} \psi_{lr}|l\rangle \otimes |r\rangle, \tag{A9}$$

where ψ_{lr} is the element of the $d_l \times d_r$ matrix ψ, $|l\rangle$ and $|r\rangle$ are the bases of the left and right half-chains, respectively. The reduced density matrix is

$$\rho_l = \text{tr}_r|\psi\rangle\langle\psi| = \sum_{r'}\langle r'|\psi\rangle\langle\psi|r'\rangle = \psi\psi^\dagger, \tag{A10}$$

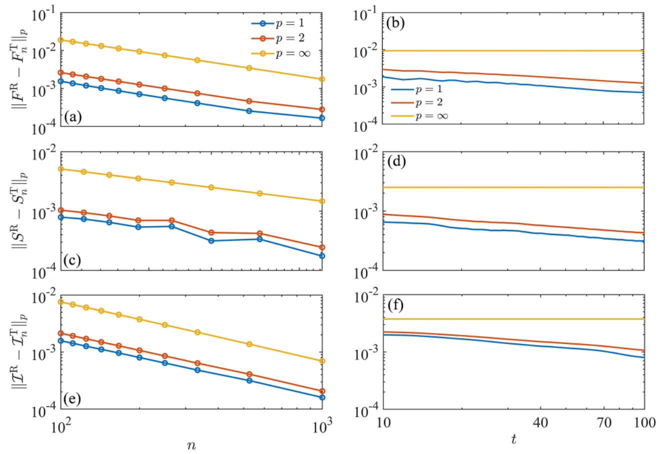

FIG. 11. Error estimates for Trotter-Suzuki decomposition. The exact values are calculated by the fourth-order Runge-Kutta method. Shown are the standard $\mathcal{L}^p$ norms of (a), (b) fidelity F; (c), (d) bipartite entanglement entropy $S_{L/2}$; and (e), (f) imbalance $\mathcal{I}$ as the function of (a), (c), (e) the Trotter steps n or (b), (d), (f) time t.

and similarly $\rho_r = (\psi^\dagger\psi)^T$. Using the singular value decomposition, we obtain the matrix ψ as

$$\psi = A\Sigma B^\dagger, \tag{A11}$$

where Σ is a $d_l \times d_r$ diagonal matrix, and A and B are $d_l \times d_l$ and $d_r \times d_r$ unitary matrices, respectively. When the lattice number L is even, we have $d_l = d_r = 2^L$ and the bipartite von Neumann entanglement entropy is

$$S_{L/2} = S_l = S_r = -\sum_{i=1}^{d_l}\Sigma_i^2 \ln \Sigma_i^2. \tag{A12}$$

The Trotter-Suzuki decomposition leads to error accumulation, but the error decreases with increased time steps n in per time unit τ. The error can be quantified by the standard $\mathcal{L}^p$ norm

$$\left\|\mathcal{O}^{\text{R}} - \mathcal{O}^{\text{T}}_n\right\|_p = \left(\int_0^t \left|\mathcal{O}^{\text{R}}(t) - \mathcal{O}^{\text{T}}_n(t)\right|^p dt\right)^{1/p}, \tag{A13}$$

with $p = 1, 2, ..., \infty$, where $\mathcal{O}$ is some physical quantity, $\mathcal{O}^{\text{R}}$ represents the exact value calculated by the fourth-order Runge-Kutta method, and $\mathcal{O}^{\text{T}}_n$ is the value calculated by the n-step Trotter-Suzuki decomposition. Specifically, $p = 1$ means the average difference between $\mathcal{O}^{\text{T}}_n$ and $\mathcal{O}^{\text{R}}$ and $= \infty$ with

$$\left\|\mathcal{O}^{\text{R}} - \mathcal{O}^{\text{T}}_n\right\|_\infty = \max\left(\left|\mathcal{O}^{\text{R}}(t) - \mathcal{O}^{\text{T}}_n(t)\right|\right)$$

means the largest difference between them. Figures 11(a) and 11(b) show $\mathcal{L}^p$ norms with $p = 1, 2, \infty$ of the fidelity F for different time step n with the fixed integration upper bound $t = 100\tau$, and for different upper bound t for a fixed time steps $n = 200$, respectively. Figures 11(c)–11(f), respectively, display the corresponding $\mathcal{L}^p$ norms for the bipartite von Neumann entanglement entropy $S_{L/2}$ and the imbalance $\mathcal{I} = (N_o - N_e)/(N_o + N_e)$ on the even and odd sublattices. In an approximate sense, the $\mathcal{L}^p$ norm approaches zero as $1/n$, and decreases slightly for increasing time.

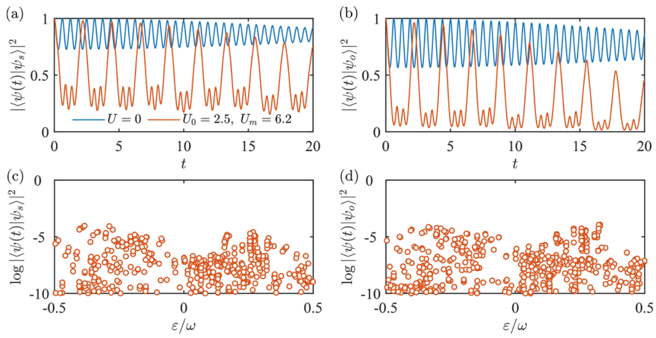

FIG. 12. Properties of the transition state encircled by black curves in Fig. 5(a). The parameters are $(U_0, U_m, \omega) = (2.5, 6.2, 2\sqrt{2})$. (a), (b) Dynamics of the wave function fidelity in a quench process from the initial state (a) $|\psi_s\rangle$ or (b) $|\psi_{th}\rangle$. Wannier-Stark localization with $U = 0$ is colored in blue and the transition state is colored in orange. (c), (d) The overlap of the Floquet eigenstates with (c) $|\psi_s\rangle$ or (d) $|\psi_{th}\rangle$.

APPENDIX B: WANNIER-STARK LOCALIZATION

For a noninteracting system with $U = 0$, the Hamiltonian can be diagonalized as [54]

$$H = \sum_{m,\sigma=\uparrow,\downarrow} \Delta m \hat{b}^\dagger_{m,\sigma} \hat{b}_{m,\sigma} + \text{H.c.} \tag{B1}$$

by the transformation

$$\hat{b}_m = \sum_{j,\sigma=\uparrow,\downarrow} \mathcal{J}_{j-m}(2J/\Delta)\hat{c}_{j,\sigma}, \tag{B2}$$

where $\mathcal{J}_n$ is the Bessel function of the first kind. Since $|\mathcal{J}_n(2J/\Delta)| < e^{-|n|}$ for $2J/\Delta \ll n$, all eigenstates are localized for any $\Delta \neq 0$: the phenomenon of called Wannier-Stark localization [55]. More specifically, each eigenstate is localized about site m with an inverse localization length

$$\xi^{-1} \approx 2\sinh^{-1}(\Delta/2J)$$

and exhibits Bloch oscillations [56,57] with the characteristic period $T = h/\Delta = 2\pi\tau/\Delta$ in our units. The wave function fidelity oscillates about a high value, as shown in blue in Figs. 12(a) and 12(b). This is a manifestation of Bloch oscillations of the period $T \approx 0.628$, in consistence with the theoretical result.

In Figs. 12(a)–12(d), the orange represents the case in the regions encircled by the black curves in Fig. 5(a): $\omega = 2\sqrt{2}$, $U_0 = 2.5$, and $U_m = 6.2$. The fidelity oscillates about a value that decays slowly over time. It does not decrease to zero and so does not indicate a revival behavior. In addition, there is no intrinsic difference between the initial states $|\psi_s\rangle$ and $|\psi_{th}\rangle$, for both the quantum fidelity [Figs. 12(a) and 12(b)] and the overlap of Floquet eigenstates with the initial states [Figs. 12(c) and 12(d)]. Especially in Fig. 12(c), the tower structure and the anomalously high overlap with $|\psi_s\rangle$ do not exist. While both the average fidelity $\langle F_s\rangle_t$ from $|\psi_s\rangle$ and the relative discrepancy ϱ are high, none of the above characteristics are consistent with the scarring dynamics. In this regard, these regions encircled by black curves in Figs. 5(a) and 5(b) correspond to the transition states from Wannier-Stark localization to the Floquet scarring phase.

APPENDIX C: FLOQUET PERTURBATION THEORY

Here we introduce the Floquet perturbation theory [27]. The Hamiltonian $H(t) = H_0(t) + V$ has the period T, where V is the time-independent perturbation term. Assuming that $H_0(t)$ commutes with itself at different times, its eigenstates $|m\rangle$ are time independent in the specific basis, as the result of $H_0(t)\,|m\rangle = E_m(t)\,|m\rangle$ and $\langle q|m\rangle = \delta_{qm}$. We also assume that V is completely off-diagonal in this basis, i.e., $\langle m|V|m\rangle = 0$ for all $|m\rangle$.

The Floquet modes $|m(t)\rangle$ of $H(t)$ satisfy the Schrödinger equation:

$$\mathrm{i}\frac{\partial|m(t)\rangle}{\partial t} = H(t)|m(t)\rangle \tag{C1}$$

and

$$|m(T)\rangle = e^{-\mathrm{i}\varepsilon_m}\,|m(0)\rangle\,, \tag{C2}$$

where ε_m are quasienergies of $H(t)$, and ε_m are eigenvalues of the Floquet Hamiltonian H_F: $H_\mathrm{F}\,|m\rangle = \varepsilon_m\,|m\rangle$. For $t = 0$, the Floquet modes $|m(0)\rangle$ are referred to as the Floquet eigenstates, which are indeed equivalent to the eigenstates $|m\rangle$. For $V = 0$, we have

$$|m(t)\rangle = e^{-\mathrm{i}\int_0^t dt' E_m(t')}\,|m\rangle\,,$$
$$e^{-\mathrm{i}\varepsilon_m} = e^{-\mathrm{i}\int_0^T dt E_m(t)}.$$

For small V, the Floquet modes $|m(t)\rangle$ can be expanded in terms of the unperturbed eigenstates:

$$|m(t)\rangle = \sum_q c_q(t)e^{-\mathrm{i}\int_0^t dt' E_q(t')}\,|q\rangle\,, \tag{C3}$$

where $c_m(t) \simeq 1$ for all t, and $c_q(t)$ is of the order V for all $q \neq m$ and all t. Substituting Eq. (C3) into the Schrödinger equation, we obtain

$$\mathrm{i}\sum_q \frac{dc_q(t)}{dt}e^{-\mathrm{i}\int_0^t dt' E_q(t')}\,|q\rangle = V\sum_q c_q(t)e^{-\mathrm{i}\int_0^t dt' E_q(t')}\,|q\rangle\,.$$

Taking the inner product with $\langle m|$ leads to

$$\mathrm{i}\frac{dc_m(t)}{dt} = c_m(t)\,\langle m|V|m\rangle + \sum_{q\neq m} c_q(t)e^{\mathrm{i}\int_0^t dt'[E_m(t')-E_q(t')]}\,\langle m|V|q\rangle\,. \tag{C4}$$

Since $\langle m|V|q\rangle$ and $c_q(t)$ are of the order V, their product in the sum represents a second-order term in V that can be neglected. Since $\langle m|V|m\rangle = 0$, we have $dc_m(t)/dt = 0$. Consequently, $c_m(t)$ can be chosen as one for all t. We get

$$|m(t)\rangle = e^{-\mathrm{i}\int_0^t dt' E_m(t')}\,|m\rangle + \sum_{q\neq m} c_q(t)e^{-\mathrm{i}\int_0^t dt' E_q(t')}\,|q\rangle\,, \tag{C5}$$

where $c_q(t)$ is of the order V for all $q \neq m$ and all t.

Taking the inner product with $\langle q(t)|$ and integrating the Schrödinger equation (C1) from $t = 0$ to $t = T$, we obtain

$$c_q(T) = c_q(0) - \mathrm{i}\,\langle q|V|m\rangle \int_0^T dt e^{\mathrm{i}\int_0^t dt'[E_q(t')-E_m(t')]}. \tag{C6}$$

In addition, utilizing the relation (C2) for all $q \neq m$, we get

$$c_q(T) = e^{\mathrm{i}\int_0^T dt[E_q(t)-E_m(t)]} c_q(0). \tag{C7}$$

Combining Eqs. (C6) and (C7), we have

$$c_q(0) = -\mathrm{i}\,\langle q|V|m\rangle \frac{\int_0^T dt e^{\mathrm{i}\int_0^t dt'[E_q(t')-E_m(t')]}}{e^{\mathrm{i}\int_0^T dt[E_q(t)-E_m(t)]} - 1}. \tag{C8}$$

The analysis so far holds for nondegenerate states. It breaks down when degeneracy occurs under the condition

$$e^{\mathrm{i}\int_0^T dt[E_q(t)-E_m(t)]} = 1. \tag{C9}$$

Suppose that there are p states satisfying the condition (C9) with $|m\rangle$, denoted as $|m_i\rangle$ with $i = 1, 2, \cdots, p$ and $|m\rangle \equiv |m_0\rangle$. Ignoring all other states of the system for the moment, the Floquet mode $|m_i(t)\rangle$ now is

$$|m_i(t)\rangle = \sum_{j=0}^{p} c_j(t) e^{-\mathrm{i}\int_0^t dt' E_j(t')} |m_j\rangle \tag{C10}$$

for $i = 0, 1, \cdots, p$, where all the $c_j(t)$'s are of the order one (not of the order V). Equation (C4) becomes

$$\mathrm{i}\frac{dc_i(t)}{dt} = \sum_{j\neq i} c_j(t) e^{\mathrm{i}\int_0^t dt'[E_i(t')-E_j(t')]} \langle m_i|V|m_j\rangle, \tag{C11}$$

where the sum term is no longer a second-order term in V. To the first order of V, we can replace $c_j(t)$ by $c_j(0)$ on the right side of Eq. (C11). Integrating from $t = 0$ to $t = T$, we have

$$c_i(T) = c_i(0) - \mathrm{i}\sum_{j\neq i} \langle m_i|V|m_j\rangle\, c_j(0) \times \int_0^T dt e^{\mathrm{i}\int_0^t dt'[E_i(t')-E_j(t')]},$$

which can be written as matrix form as

$$c(T) = (I - \mathrm{i}M)c(0), \tag{C12}$$

where $c(t) = [c_0(t), c_1(t), \cdots, c_p(t)]^T$ and the $(p+1)\times(p+1)$ matrix M has the elements

$$M_{ij} = \langle m_i|V|m_j\rangle \int_0^T dt e^{\mathrm{i}\int_0^t dt'[E_i(t')-E_j(t')]}. \tag{C13}$$

Let the eigenvalues of M be ς_i with $i = 0, 1, \cdots, p$. The corresponding eigenstates are $c(T) = e^{-\mathrm{i}\varsigma_i} c(0)$. The Floquet modes $|m_i(t)\rangle$ satisfy the condition

$$|m_i(T)\rangle = e^{-\mathrm{i}\varepsilon_i T} |m_i(0)\rangle.$$

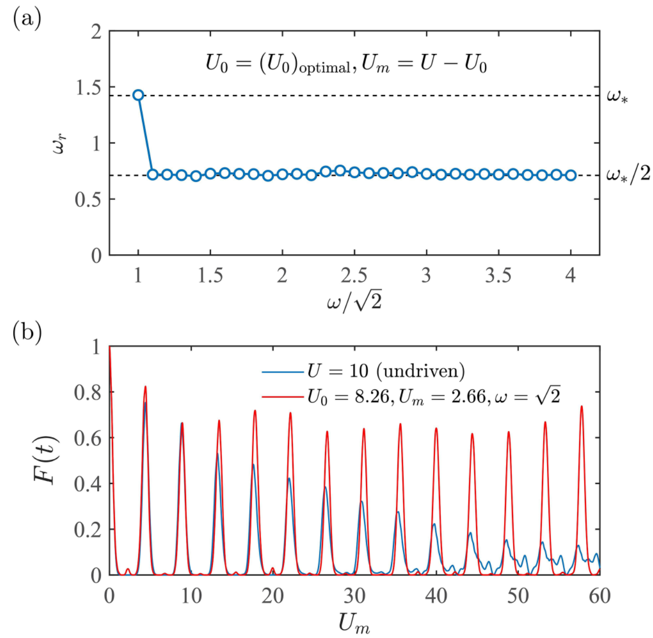

FIG. 13. Period doubling of quantum revival under square-wave drive. (a) Period doubling occurred for $U_0 = (U_0)_{\text{optimal}}$ and $U_m = U - U_0$, for $U = 10$. (b) Driven quantum revival from $|\psi_s\rangle$, which is enhanced and stabilized by the square-wave driving, for optimal parameter set $(U_0, U_m, \omega) = (8.26, 2.66, \sqrt{2})$.

The Floquet quasienergies are then given by

$$e^{-\mathrm{i}\varepsilon_i T} = e^{-\mathrm{i}\varsigma_i - \mathrm{i}\int_0^T dt E_i(t)}, \tag{C14}$$

and the Floquet Hamiltonian is

$$(H_{\mathrm{F}})_{ij} = \frac{M_{ij}}{T}. \tag{C15}$$

APPENDIX D: ROBUST PERIOD DOUBLING

In contrast to the tunable responses, there is a robust period-doubling phenomenon relating the driven and undriven revival periods: $T_r = 2T_*$ for $U_0 = (U_0)_{\text{optimal}}$ and $U_m = U - U_0$, as exemplified in Fig. 2(a). Figure 13(a) shows such a phenomenon for $\omega_r \approx \omega_*/2$ over a wide range of ω. For $\omega = \sqrt{2}$, there is a harmonic response: $T_r \approx T_*$. In this case, we have identified an overall optimal parameter set $(\omega, U_0, U_m) = (\sqrt{2}, 8.26, 2.66)$ for 31 values of the driving frequency, in which the quantum revival is greatly enhanced and stabilized by periodic driving, especially for a long-time evolution, as shown in Fig. 13(b). The optimal driving frequency is close to the undriven revival frequency: $\omega_{\text{optimal}} \approx \omega_*$, and the driven revival frequency is close to the optimal driving frequency: $\omega_r \approx \omega_{\text{optimal}}$ (the harmonic response).

[1] H. Bernien, S. Schwartz, A. Keesling, H. Levine, A. Omran, H. Pichler, S. Choi, A. S. Zibrov, M. Endres, M. Greiner *et al.*, Probing many-body dynamics on a 51-atom quantum simulator, Nature (London) **551**, 579 (2017).

[2] M. Serbyn, D. A. Abanin, and Z. Papić, Quantum many-body scars and weak breaking of ergodicity, Nat. Phys. **17**, 675 (2021).

[3] C. J. Turner, A. A. Michailidis, D. A. Abanin, M. Serbyn, and Z. Papić, Weak ergodicity breaking from quantum many-body scars, Nat. Phys. **14**, 745 (2018).

[4] C. J. Turner, A. A. Michailidis, D. A. Abanin, M. Serbyn, and Z. Papić, Quantum scarred eigenstates in a Rydberg atom chain: Entanglement, breakdown of thermalization, and stability to perturbations, Phys. Rev. B **98**, 155134 (2018).

[5] T. Iadecola, M. Schecter, and S. Xu, Quantum many-body scars from magnon condensation, Phys. Rev. B **100**, 184312 (2019).
[6] W. W. Ho, S. Choi, H. Pichler, and M. D. Lukin, Periodic orbits, entanglement, and quantum many-body scars in constrained models: Matrix product state approach, Phys. Rev. Lett. **122**, 040603 (2019).
[7] C.-J. Lin and O. I. Motrunich, Exact quantum many-body scar states in the Rydberg-blockaded atom chain, Phys. Rev. Lett. **122**, 173401 (2019).
[8] K. Bull, J.-Y. Desaules, and Z. Papić, Quantum scars as embeddings of weakly broken lie algebra representations, Phys. Rev. B **101**, 165139 (2020).
[9] C.-J. Lin, A. Chandran, and O. I. Motrunich, Slow thermalization of exact quantum many-body scar states under perturbations, Phys. Rev. Res. **2**, 033044 (2020).
[10] C. J. Turner, J.-Y. Desaules, K. Bull, and Z. Papić, Correspondence principle for many-body scars in ultracold Rydberg atoms, Phys. Rev. X **11**, 021021 (2021).
[11] S. Moudgalya, S. Rachel, B. A. Bernevig, and N. Regnault, Exact excited states of nonintegrable models, Phys. Rev. B **98**, 235155 (2018).
[12] S. Moudgalya, N. Regnault, and B. A. Bernevig, Entanglement of exact excited states of Affleck-Kennedy-Lieb-Tasaki models: Exact results, many-body scars, and violation of the strong eigenstate thermalization hypothesis, Phys. Rev. B **98**, 235156 (2018).
[13] D. K. Mark, C.-J. Lin, and O. I. Motrunich, Unified structure for exact towers of scar states in the Affleck-Kennedy-Lieb-Tasaki and other models, Phys. Rev. B **101**, 195131 (2020).
[14] S. Moudgalya, E. O'Brien, B. A. Bernevig, P. Fendley, and N. Regnault, Large classes of quantum scarred Hamiltonians from matrix product states, Phys. Rev. B **102**, 085120 (2020).
[15] S. Moudgalya, N. Regnault, and B. A. Bernevig, η-pairing in Hubbard models: From spectrum generating algebras to quantum many-body scars, Phys. Rev. B **102**, 085140 (2020).
[16] A. Hudomal, I. Vasić, N. Regnault, and Z. Papić, Quantum scars of bosons with correlated hopping, Commun. Phys. **3**, 99 (2020).
[17] J.-Y. Desaules, A. Hudomal, C. J. Turner, and Z. Papić, Proposal for realizing quantum scars in the tilted 1D Fermi-Hubbard model, Phys. Rev. Lett. **126**, 210601 (2021).
[18] Q. Hummel, K. Richter, and P. Schlagheck, Genuine many-body quantum scars along unstable modes in Bose-Hubbard systems, Phys. Rev. Lett. **130**, 250402 (2023).
[19] L.-L. Ye and Y.-C. Lai, Controlling nonergodicity in quantum many-body systems by reinforcement learning, Phys. Rev. Res. **7**, 013256 (2025).
[20] J.-L. Ma, Z. Guo, Y. Gao, Z. Papić, and L. Ying, Liouvillean spectral transition in noisy quantum many-body scars, arXiv:2504.12291.
[21] P. Zhang, H. Dong, Y. Gao, L. Zhao, J. Hao, J.-Y. Desaules, Q. Guo, J. Chen, J. Deng, B. Liu *et al.*, Many-body Hilbert space scarring on a superconducting processor, Nat. Phys. **19**, 120 (2023).
[22] J. Ren, A. Hallam, L. Ying, and Z. Papić, Scarfinder: A detector of optimal scar trajectories in quantum many-body dynamics, arXiv:2504.12383.
[23] J. M. Deutsch, Quantum statistical mechanics in a closed system, Phys. Rev. A **43**, 2046 (1991).
[24] M. Srednicki, Chaos and quantum thermalization, Phys. Rev. E **50**, 888 (1994).
[25] M. Rigol, V. Dunjko, and M. Olshanii, Thermalization and its mechanism for generic isolated quantum systems, Nature (London) **452**, 854 (2008).
[26] D. Bluvstein, A. Omran, H. Levine, A. Keesling, G. Semeghini, S. Ebadi, T. T. Wang, A. A. Michailidis, N. Maskara, W. W. Ho *et al.*, Controlling quantum many-body dynamics in driven Rydberg atom arrays, Science **371**, 1355 (2021).
[27] B. Mukherjee, S. Nandy, A. Sen, D. Sen, and K. Sengupta, Collapse and revival of quantum many-body scars via Floquet engineering, Phys. Rev. B **101**, 245107 (2020).
[28] K. Mizuta, K. Takasan, and N. Kawakami, Exact Floquet quantum many-body scars under Rydberg blockade, Phys. Rev. Res. **2**, 033284 (2020).
[29] S. Sugiura, T. Kuwahara, and K. Saito, Many-body scar state intrinsic to periodically driven system, Phys. Rev. Res. **3**, L012010 (2021).
[30] B. Mukherjee, A. Sen, D. Sen, and K. Sengupta, Dynamics of the vacuum state in a periodically driven Rydberg chain, Phys. Rev. B **102**, 075123 (2020).
[31] A. Hudomal, J.-Y. Desaules, B. Mukherjee, G.-X. Su, J. C. Halimeh, and Z. Papić, Driving quantum many-body scars in the PXP model, Phys. Rev. B **106**, 104302 (2022).
[32] K. Huang and X. Li, Engineering subharmonic responses beyond prethermalization via Floquet scar states, Phys. Rev. B **109**, 064306 (2024).
[33] H. Zhao, J. Vovrosh, F. Mintert, and J. Knolle, Quantum many-body scars in optical lattices, Phys. Rev. Lett. **124**, 160604 (2020).
[34] B. Mukherjee, A. Sen, D. Sen, and K. Sengupta, Restoring coherence via aperiodic drives in a many-body quantum system, Phys. Rev. B **102**, 014301 (2020).
[35] G.-X. Su, H. Sun, A. Hudomal, J.-Y. Desaules, Z.-Y. Zhou, B. Yang, J. C. Halimeh, Z.-S. Yuan, Z. Papić, and J.-W. Pan, Observation of many-body scarring in a Bose-Hubbard quantum simulator, Phys. Rev. Res. **5**, 023010 (2023).
[36] L. Beringer, M. Steinhuber, J. D. Urbina, K. Richter, and S. Tomsovic, Controlling many-body quantum chaos: Bose-Hubbard systems, New J. Phys. **26**, 073002 (2024).
[37] N. Maskara, A. A. Michailidis, W. W. Ho, D. Bluvstein, S. Choi, M. D. Lukin, and M. Serbyn, Discrete time-crystalline order enabled by quantum many-body scars: Entanglement steering via periodic driving, Phys. Rev. Lett. **127**, 090602 (2021).
[38] B. Huang, T.-H. Leung, D. M. Stamper-Kurn, and W. V. Liu, Discrete time crystals enforced by Floquet-Bloch scars, Phys. Rev. Lett. **129**, 133001 (2022).
[39] B. Huang, Analytical theory of cat scars with discrete time-crystalline dynamics in Floquet systems, Phys. Rev. B **108**, 104309 (2023).
[40] S. Pai and M. Pretko, Dynamical scar states in driven fracton systems, Phys. Rev. Lett. **123**, 136401 (2019).
[41] A. Haldar, D. Sen, R. Moessner, and A. Das, Dynamical freezing and scar points in strongly driven Floquet matter: Resonance vs emergent conservation laws, Phys. Rev. X **11**, 021008 (2021).
[42] P.-G. Rozon, M. J. Gullans, and K. Agarwal, Constructing quantum many-body scar Hamiltonians from Floquet automata, Phys. Rev. B **106**, 184304 (2022).

[43] M. Ljubotina, E. Petrova, N. Schuch, and M. Serbyn, Tangent space generators of matrix product states and exact Floquet quantum scars, PRX Quantum **5**, 040311 (2024).

[44] S. Scherg, T. Kohlert, P. Sala, F. Pollmann, B. Hebbe Madhusudhana, I. Bloch, and M. Aidelsburger, Observing non-ergodicity due to kinetic constraints in tilted Fermi-Hubbard chains, Nat. Commun. **12**, 4490 (2021).

[45] T. Kohlert, S. Scherg, P. Sala, F. Pollmann, B. Hebbe Madhusudhana, I. Bloch, and M. Aidelsburger, Exploring the regime of fragmentation in strongly tilted Fermi-Hubbard chains, Phys. Rev. Lett. **130**, 010201 (2023).

[46] Z. Papić, Weak ergodicity breaking through the lens of quantum entanglement, in *Entanglement in Spin Chains: From Theory to Quantum Technology Applications* (Springer International Publishing, Cham, 2022), pp. 341–395.

[47] P. Courteille, R. S. Freeland, D. J. Heinzen, F. A. van Abeelen, and B. Verhaar, Observation of a Feshbach resonance in cold atom scattering, Phys. Rev. Lett. **81**, 69 (1998).

[48] C. Chin, R. Grimm, P. Julienne, and E. Tiesinga, Feshbach resonances in ultracold gases, Rev. Mod. Phys. **82**, 1225 (2010).

[49] X. W. Wang, E. Khatami, F. Fei, J. Wyrick, P. Namboodiri, R. Kashid, A. F. Rigosi, G. Bryant, and R. Silver, Experimental realization of an extended Fermi-Hubbard model using a 2D lattice of dopant-based quantum dots, Nat. Commun. **13**, 6824 (2022).

[50] M. Bukov, L. D'Alessio, and A. Polkovnikov, Universal high-frequency behavior of periodically driven systems: From dynamical stabilization to Floquet engineering, Adv. Phys. **64**, 139 (2015).

[51] A. Soori and D. Sen, Nonadiabatic charge pumping by oscillating potentials in one dimension: Results for infinite system and finite ring, Phys. Rev. B **82**, 115432 (2010).

[52] J. J. Sakurai, *Advanced Quantum Mechanics* (Addison-Wesley, Menlopark, 1967).

[53] J.-Y. Huang, Floquet quantum many-body scars in the tilted Fermi-Hubbard chain, Zenodo, 2025, https://zenodo.org/records/15773408.

[54] E. van Nieuwenburg, Y. Baum, and G. Refael, From Bloch oscillations to many-body localization in clean interacting systems, Proc. Natl. Acad. Sci. USA **116**, 9269 (2019).

[55] G. H. Wannier, Wave functions and effective Hamiltonian for Bloch electrons in an electric field, Phys. Rev. **117**, 432 (1960).

[56] M. Ben Dahan, E. Peik, J. Reichel, Y. Castin, and C. Salomon, Bloch oscillations of atoms in an optical potential, Phys. Rev. Lett. **76**, 4508 (1996).

[57] L.-L. Ye and Y.-C. Lai, Irregular Bloch-Zener oscillations in two-dimensional flat-band dirac materials, Phys. Rev. B **107**, 165422 (2023).